

<https://doi.org/10.1038/s43246-025-00803-5>

Improving multifunctional monolithic nano-device by single (Al,Ga)N nanowire/graphene van der Waals heterostructure for neuromorphic computing, photodetection and imaging

Check for updates

Min Zhou^{1,7}, Min Jiang^{1,7}, Chaoyun Song^{1,2}✉, Kai Xu², Zexin Yu³, Lifeng Bian⁴, Liubin Yang¹, Jianya Zhang⁵✉, Shulong Lu^{1,6}✉ & Yukun Zhao^{1,6}✉

Integrating neuromorphic computing, photodetection and imaging in single devices remains challenging due to the inherent trade-off between the transient photoresponse speeds of artificial synapses and photodetectors. This study develops a dual-mode monolithic device using a (Al,Ga)N nanowire/graphene heterojunction, operating as a photodetector under negative bias and a neuromorphic sensor under positive bias. Graphene strengthens the built-in electric field, enhancing carrier separation and photocurrent for both functions. The device consumes ultralow energy (3.19×10^{-11} J) with demonstrated synaptic plasticity features like spike-dependent learning and accelerated memory reinforcement. Leveraging this synaptic plasticity, the device achieves over 90% accuracy in image processing tasks. This work introduces a multifunctional integration strategy that advances neuromorphic computing efficiency and optoelectronic device design, demonstrating the feasibility of simultaneous imaging and brain-inspired computation in compact systems.

Combining multiple functionalities within a single optoelectronic device is crucial for the next-generation optoelectronics, including the neuromorphic computing, photodetection, and imaging^{1,2}. Photodetectors (PDs) are essential components in a variety of optoelectronic applications, including photodetection, imaging technologies, and optical communication systems, which play a pivotal role in harnessing visual information^{3,4}. By capturing light signals and converting them into electronic signals, PDs enables machines to perceive and interpret their environments, analogous to human visual perception^{5,6}. The human visual system, comprising the ocular apparatus and the central nervous system, has undergone extensive evolution to adeptly capture and process intricate visual stimuli^{7,8}. This capability enables the formation of memories that can be easily retrieved at a later time, playing a critical role in our daily functioning and decision-making⁹.

Inspired by biological systems, researchers are currently investigating and developing a neuromorphic visual sensor (NVS) that mimics the physiological mechanisms of the human eye. This innovative sensor is designed to facilitate the perception, memory and processing of light signals, thereby enabling advanced interpretations of photonic information^{9–12}. However, a notable limitation of PD is their inability to store and promptly recall historical visual information¹³. Thus, it is urgent to develop a machine visual system that integrates multiple functions, specifically the incorporation of PDs and NVS within a single device.

GaN-based materials are progressively being acknowledged for their considerable potential in the fields of photodetection and neuromorphic engineering^{14,15}. Nanowires (NWs) have a topology analogous to that of tubular axons, which significantly influences the processing of data in

¹Division of Nano-Devices Research, Suzhou Institute of Nano-Tech and Nano-Bionics (SINANO), Chinese Academy of Sciences (CAS), Suzhou, China.

²Department of Engineering, King's College London, London, UK. ³Institute for Manufacturing Technologies of Ceramic Components and Composites, University of Stuttgart, Stuttgart, Germany. ⁴Frontier Institute of Chip and System, Fudan University, Shanghai, China. ⁵Key Laboratory of Intelligent Optoelectronic Devices and Chips of Jiangsu Higher Education Institutions, School of Physical Science and Technology, Suzhou University of Science and Technology, Suzhou, China.

⁶School of Nano-Tech and Nano-Bionics, University of Science and Technology of China, Hefei, China. ⁷These authors contributed equally: Min Zhou, Min Jiang.

✉ e-mail: chaoyun.song@kcl.ac.uk; jy Zhang2022@usts.edu.cn; sllu2008@sinano.ac.cn; ykzhao2017@sinano.ac.cn

biological systems^{16–18}. When coupled with their significant surface area, efficient transport of charge and high light responsiveness to particular wavelength ranges, nanowires can modulate synaptic activity with increased flexibility while consuming low power^{19–23}. In addition, GaN nanowires boost light-material contact area and absorption efficiency by prolonging light paths, enhancing photoelectric conversion^{17,18}. Due to the high surface-to-volume ratio of a single nanowire, its surface effects become more pronounced in ultra-small volumes, facilitating the effective modulation of its photoelectric response characteristics for fabricating various types of devices^{24,25}. Furthermore, the device based on a single nanowire is much smaller in volume compared to traditional devices, enabling a significant reduction in the size of the overall system^{24,25}. In situ integration methods for multifunctional device can simplify the fabrication process, making it feasible to produce large-scale, uniform hybrid structures with improved compatibility²⁶. Hence, it is very promising to prepare multifunctional device based on GaN-based nanowires, which can make the supporting systems much simpler and expand the application scenarios greatly. However, synaptic devices require more time for signal processing and storage, while PDs typically rely on fast light response capabilities^{27,28}. In other words, their requirements for light response speeds have significant contradiction, making it quite difficult to integrate them into a single monolithic device.

In addition, although a single-nanowire device has the very small size and it is beneficial for integration, the photocurrent is very low, which severely hinders its development²⁹. It is challenging to improve the performance of the single-nanowire device with multiple functions. In this work, we propose a multifunctional device achieved through the successful construction of a van der Waals heterojunction between a single (Al,Ga)N nanowire and graphene. We overcome the contradiction of response speeds for PDs and neuromorphic visual sensor by modulating the bias voltage to switch between different functions. This type of heterojunction device can improve the light response current and excitatory postsynaptic current (EPSC) compared with a single nanowire device. Additionally, the device can emulate several synaptic functions, including paired pulse facilitation (PPF), spike-number-dependent plasticity (SNDP), spike-frequency-dependent plasticity (SFDP) and spike-intensity-dependent plasticity (SIDP), as well as exhibiting learning behavior. It results in a significant enhancement of the recognition accuracy and efficiency of the neuro-visual sensing processes for images, through pre-processing and non-pre-processing techniques.

Results and discussion

Design and preparation of single nanowire/graphene heterostructure

The preparation procedure is shown in Fig. 1a–d. The device is proposed to be used as the indispensable component of the human biological vision system to recognize and process images (Fig. 1e). Essentially, this involves a sample training process that allows an individual to retain and recall images. As part of this demonstration, the image of the digit “8” has been randomly extracted from a database containing numbers from 0 to 9. The synaptic structure within neurons is crucial for the process of recognizing and distinguishing numbers. When exposed to biological stimuli, the visual system activates anterior neurons to send bioelectric signals to posterior neurons via synaptic units. This transmission creates a potential difference, resulting in a EPSC³⁰. The incident light, electrodes, and photogenerated charge in the multifunctional device act as a biological spike, pre-synaptic/post-synaptic membrane, and neurotransmitter in a biological synapse, respectively³¹.

From Fig. 1f, it can be seen that the grown nanowires exhibit excellent vertical alignment and morphological uniformity, with the heights exceeding 2100 nm and diameters ranging from 60 nm to 110 nm. Figure 1g reveals a distinct GaO_x shell on the sidewall of the nanowires. According to Fig. 1h, the O and N elements further confirm the presence of GaO_x on the sidewall³². Meanwhile, the proportion of O within the material is below the precise stoichiometric ratio expected for Ga₂O₃ (Figs. 1h and S1), indicating the possible formation of O vacancies in GaO_x³³. To further investigate the underlying mechanism of native oxide-shelled single nanowire, a comprehensive analysis using X-ray photoelectron spectroscopy (XPS) are

conducted. This approach is crucial for monitoring the intricate chemical characteristics and precise binding states of the atoms in (Al,Ga)N nanowires. From Fig. 1i, it can be seen that the Ga 3d spectra are meticulously deconvoluted into three distinct peaks. The first peak (~21.24 eV) corresponds to the Ga oxide (Ga-O) bond, indicating the presence of the oxide. Similarly, the N 1s spectrum is fitted to three distinct peaks (Fig. 1j). The prominent peak observed at approximately 397.24 eV is attributed to the bonding of N-Ga, while the other two peaks at about 395.74 eV and 392.30 eV correspond to Ga LMM Auger transitions¹⁴. Meanwhile, the O 1s spectra are deconvoluted into two different peaks (Fig. 1k), which are centered at approximately 532.14 eV and 530.87 eV, corresponding to metal-oxide (M-O) and oxygen vacancy (V_O), respectively³⁴. The XPS results agree with the STEM results about the O element. The presence of V_O is crucial for the synaptic performance of the multifunctional monolithic devices.

Function as both photodetector and synaptic device

Carrier transport diagrams presented in Fig. 2a–e offer an in-depth elucidation of the working mechanisms underlying the two devices. When device A is exposed to light, photogenerated carriers (electrons and holes) are generated (Fig. 2a, c), which are subsequently separated by the electric field established at the interface between the nanowire and the Ti/Au electrode. For device B, the integration of graphene introduces a heterojunction at the interface between graphene and nanowire, expanding the width of the built-in electric field (Fig. 2b, d). Moreover, it enhances the carrier transport rate, leading to the more efficient collection of carriers. When device B is under reverse bias, the internal defects are moved away from the space charge region by the electric field (Fig. 2e). When the device is exposed to long-term light conditions, the transport and recombination processes of charge carriers occur with greater efficiency, thus exhibiting the characteristics of a PD (Fig. 2d, f). Similarly, when device B is subjected to a positive bias voltage, internal defects accumulate in the depletion region as a result of the influence of the electric field³⁵. When the device is illuminated, the defects capture the charge carriers, resulting in slower transport and recombination of charge carriers. Therefore, device B exhibits the synaptic characteristics (Fig. 2e, g).

Graphene, characterized by high carrier mobility and UV transparency, readily forms van der Waals heterojunctions (vdWH) because its surface lacks dangling bonds¹. Compared to other structural devices, heterojunction-based devices exhibit superior performance with a built-in electric field at the heterojunction interface, which facilitates the separation and transport of light-induced charge carriers¹³. As a PD, the absolute value of photocurrent of device B is much higher than that of device A (Fig. 2f and Fig. S2). As a synaptic device, device B exhibits a larger EPSC than device A when subjected to varying intervals and power densities of light pulses (Fig. 2g, h). A similar phenomenon is also observed under varying light power densities (Fig. S3). Hence, the introduction of graphene can increase the performance for both photodetection and neuromorphic computing by forming van der Waals heterojunction.

As shown in Figs. 3a–c and S3, the dynamic synaptic plasticity of device B under light stimulation is systematically measured by applying a bias of 5 V. As presented in the illustration of Fig. 3a, the intensity of the first photoresponse (A₁) is markedly lower than that of the second photoresponse (A₂). This phenomenon can be attributed to the fact that the current induced by the initial optical pulse does not completely return to the baseline before the second pulse occurs. This residual current combines with the current generated from the second pulse, creating a cumulative effect resembling the phenomenon of PPF observed in biological synapses. In addition, pulse interval time plays a critical role in amplifying the EPSC. The extracted PPF index is calculated and fitted well using the following equations:

$$PPF = \frac{I_2}{I_1} \times 100\% \quad (1)$$

$$I = C_1 e^{-t/\tau_1} + C_2 e^{-t/\tau_2} + I_0 \quad (2)$$

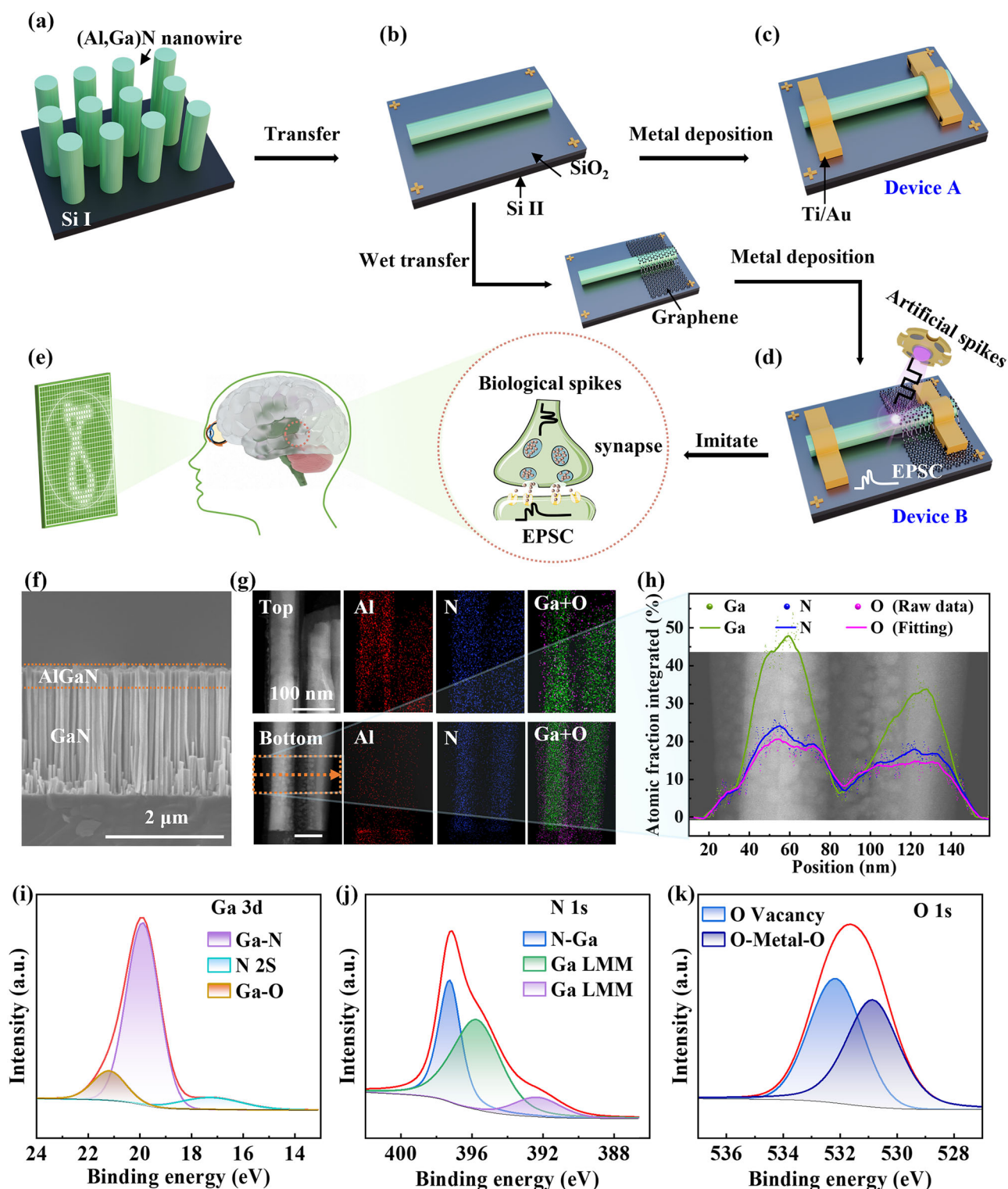


Fig. 1 | Schematic diagrams of device preparation processes and digital recognition. **a** Grow the (Al,Ga)N nanowires. **b** Transfer the nanowires onto the Si/SiO₂ substrate. **c** Ti/Au electrodes were prepared on both ends of the nanowire, completing the fabrication of device A. **d** Complete the preparation of device B by transferring graphene and depositing metal electrodes. **e** Schematic diagram of the ability of the neuro visual system to recognize images. **Experimental**

characterization of material properties. **f** SEM images of the nanowires. **g** Aberration-corrected scanning transmission electron microscopy (AC-STEM) image and high-resolution energy-dispersive X-ray (EDX) mapping of the nanowire top and bottom. **h** Distribution of the Ga, N, and O elements at the bottom of nanowires. The XPS results of device B. XPS spectra of (i) Ga 3 d, (j) N 1 s and (k) O 1 s elements within (Al,Ga)N nanowires.

I_1 and I_2 represent the intensities of the EPSC stimulated by the first and second light pulses, respectively³⁵. I_0 denotes the initial steady-state photocurrent³⁶. C_1 and C_2 are constants in the equation³⁶. t represents time. τ_1 and τ_2 refer to the fast and slow components of the photocurrent

response, respectively, corresponding to the different relaxation time constants³⁶. Specifically, τ_1 is associated with a rapid decrease in the photocurrent. The decrease results from the recombination of charge carriers, which is typically linked to inter-band transitions. On the other

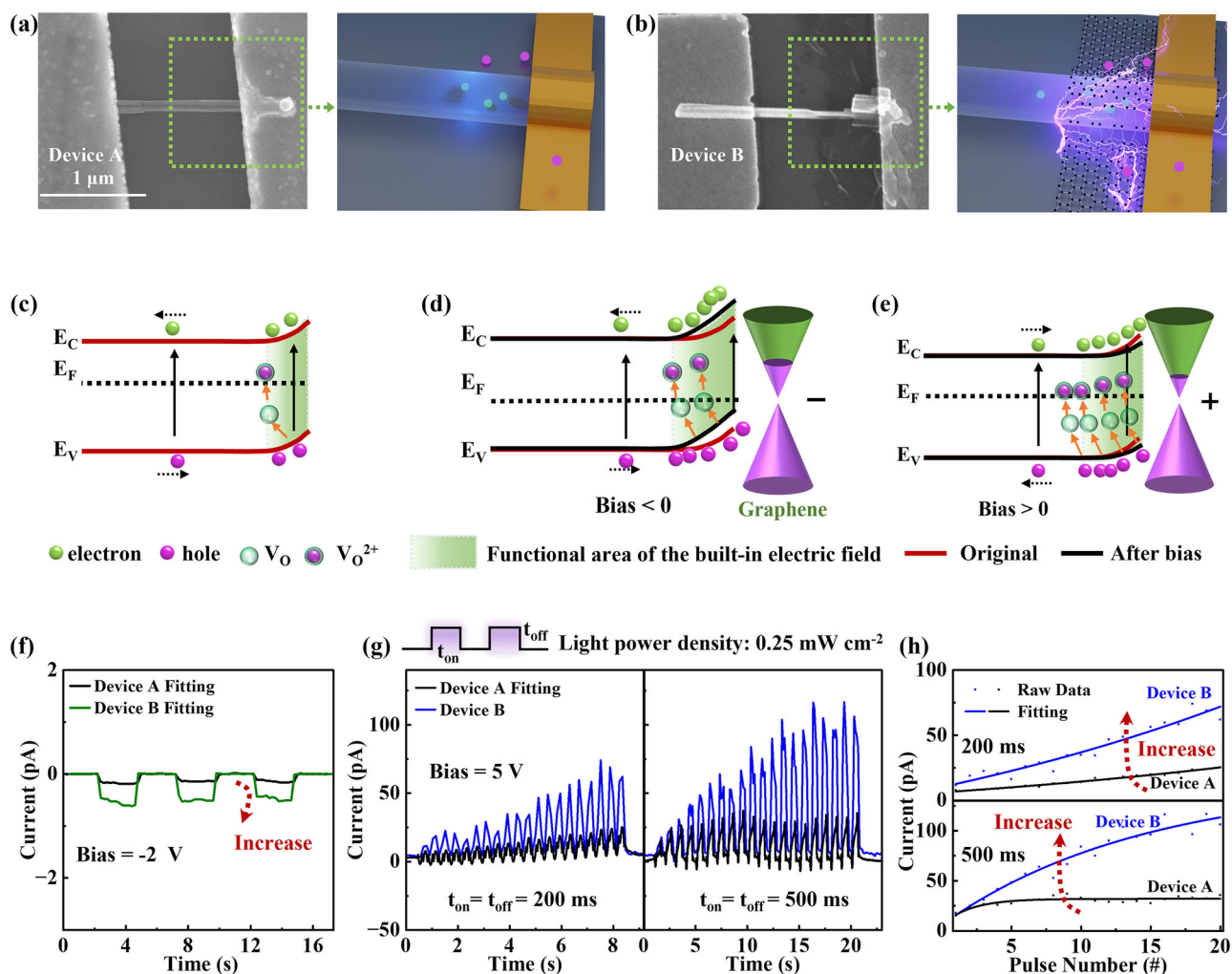


Fig. 2 | Comparison of optoelectronic performance of two devices. Top-view SEM images and schematic diagrams (a) device A and (b) device B. Energy band diagrams of (c) device A under illumination, (d) device B under negative bias and illumination, (e) device B under positive bias and illumination. **f** Comparison of photogenerated currents between devices A and B under negative bias, and the Raw Data is shown in Fig. S2a. **g** The EPSC of devices A and B triggered by 20 light pulses under positive bias, and the Raw Data is shown in Fig. S2b. **h** The extracted EPSC results of devices A and B under illumination.

hand, τ_2 is related to a more gradual reduction in the photocurrent. This slower process is attributed to the trapping of carriers, a phenomenon often associates with transitions involving defects in a material³⁶. According to Fig. 3a and Eq. (2), τ_1 and τ_2 are calculated to be 0.01 s and 16.03 s, respectively. These findings suggest that the device is a promising contender for emulating neural networks inspired by biological systems.

The effects of the number, frequency and intensity of light stimulation on synaptic plasticity are governed by distinct underlying mechanisms known as SNDP, SFDP and SIDP³⁷. Figure 3b shows the EPSC data extracted from Fig. S4a–S4c. The magnitude of EPSC is negatively correlated with the frequency of pulse stimulation. As the frequency of the light pulses decreases, a corresponding enhancement in the EPSC can be observed. This is attributed to the increased probability of neurotransmitter release and receptor activation during longer light illumination times, leading to a more potent excitatory response in postsynaptic neurons³⁸. Similarly, the magnitude of the EPSC exhibits a proportional increase in response to the number of light pulses (Figs. 3c and S3d, S3e) because a greater number of light pulses can augment the probability of neurotransmitter release, causing a more significant influx of current during subsequent pulses³⁹. Meanwhile, the impact of high temperature on synaptic plasticity has been shown in Fig. 3d, which is extracted from Fig. S5a. The EPSC declines with the increase of operating temperature, yet the synaptic behavior remained. This

means that the device has the potential to simulate synaptic behavior in some extreme environments. To evaluate the effect of the device at different voltage amplitudes, the relationship between EPSC and voltage is shown in Fig. 3e (EPSC data extracted from Fig. S5b). The results indicate that the EPSC of the device increases with the increase of voltage, which is consistent with those in Fig. 3b, c, indicating the enhancement of synaptic ability. The characteristics of device B responding to different wavelengths of light (0.25 mW cm^{-2}) are shown in Fig. 3f (EPSC data extracted from Fig. S5c). It can be found that the response signal of the device is prominent under deep-UV irradiation. The EPSC results are almost negligible in the visible range, indicating the excellent wavelength selectivity. As illustrated in Table 1, among devices utilizing GaN nanowires, very few works have been reported on the integration of photodetectors with synaptic devices, whereas the UV/visible rejection ratio in this work is superior to others without dual-functionality to some extent (Fig. 3f). Additionally, the repetitive stimulation can activate more synaptic sites, leading to a larger postsynaptic response. This enhancement in synaptic transmission reflects the brain's ability to adapt and strengthen connections based on activity levels⁴⁰.

In addition, our research delved into the remarkable capabilities of the synapse device, particularly its proficiency in emulating the 'learning-forgetting-relearning' cycle (Fig. 3g, h). This cycle closely parallels learning and memory processes observed in the human brain⁴¹. Notably, the device

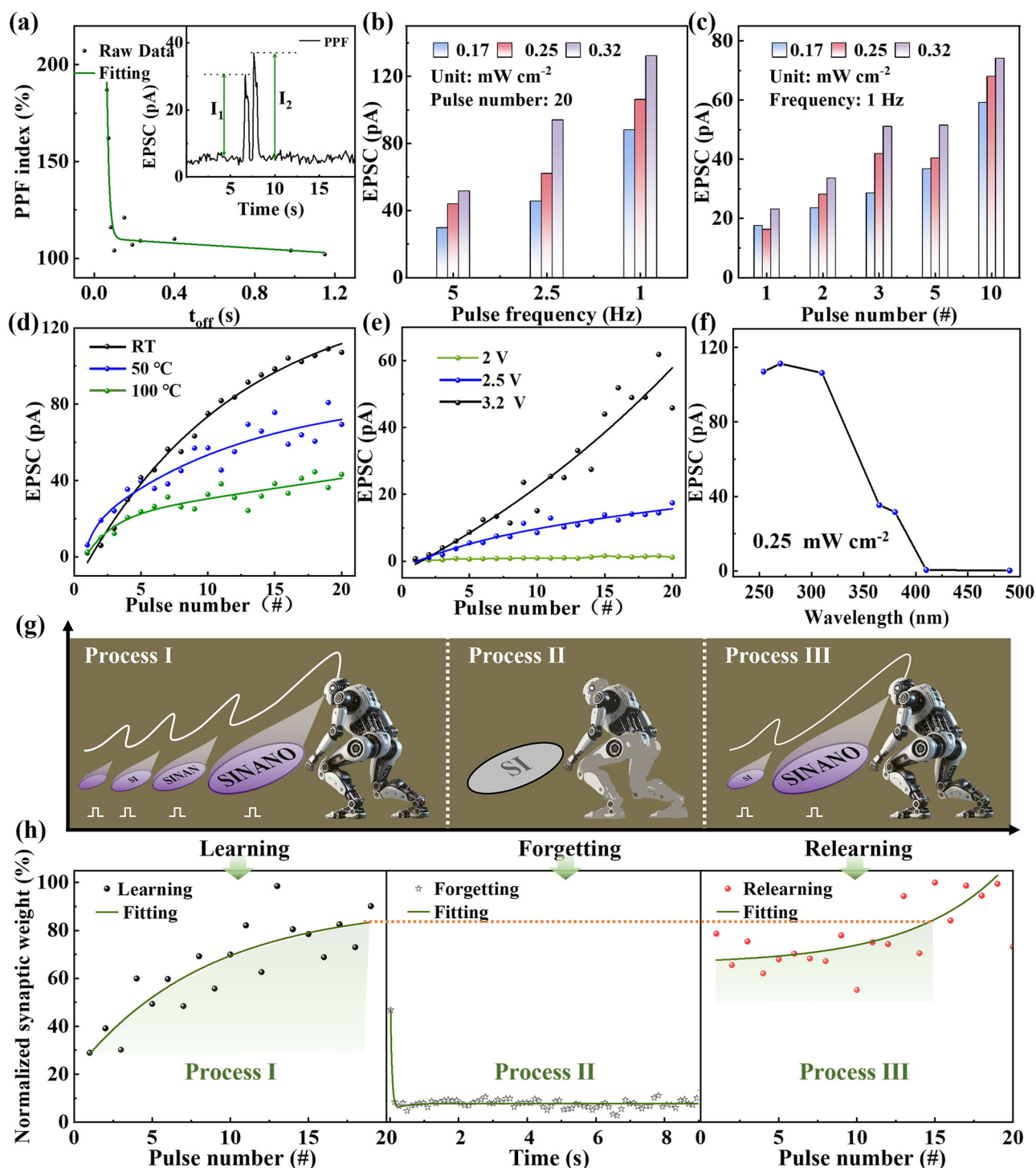


Fig. 3 | The synaptic plasticity and learning capacity of device B. **a** The PPF index of device B. The inset shows an EPSC under stimuli by two light pulses. **b** The EPSC of device B triggered by 20 light pulses at different light power densities and light pulse frequencies. **c** The EPSC of device B triggered by a 1 Hz frequency of light pulse

with different light power densities and pulse numbers. The EPSC of device B triggered by 20 light pulses at **(d)** different temperatures, **(e)** different voltage biases, and **(f)** at different light wavelengths. **g** Schematic illustration and **(h)** experimental results of the “learning-forgetting-relearning” processes.

exhibits sophisticated neural-like behavior by dynamically adjusting its synaptic strengths, thereby mimicking the brain’s ability to learn new information, gradually forgetting unused data and efficiently relearning when necessary. To demonstrate the learning ability of the device more intuitively, a schematic is plotted in Fig. 3g. Give the robot some time to learn the word ‘SINANO’ (Process I). Then take a break for a period of time, and the robot will forget the newly learned words (Process II). However, if

reviewed in a timely manner, the robot will quickly recall the words learned (Process III). This phenomenon corresponds to the learning process of the device (Fig. 3h, which illustrates that the synaptic weight (Δw) gradually increases as the number of light pulses increases, mirroring the learning mechanism of the human brain⁴². Initially, the synaptic weight increased from 28.9 to 90.2% upon receiving the 19 light pulses. Following the phase of memory lapse and relearning start, it is noted that the prior peak of synaptic

Table 1 | Comparative analysis of this work and some other recently reported works

Materials	Photodetector/ Synaptic device integrated	Energy consumption (10^{-11} J)	UV/visible rejection ratio	Refs.
Graphene/ (Al,Ga)N NWs	Yes/Yes	3.19	445	This work
p-GaN/ (In,Ga)N NWs	Yes/Yes	22.5	/	2
GaN/Ga ₂ O ₃ / GaN NWs	Yes/Yes	58.4	/	52
GaN Film	No/Yes	3.34	/	14
InAs NWs	No/Yes	1.25	/	47
ZnO NWs	No/Yes	1×10^5	/	48
Si NWs	No/Yes	1×10^2	/	49
GaN NWs	No/Yes	0.272	/	29
TiO ₂ NWs	No/Yes	13	/	50
(Al,Ga)N NWs	Yes/No	/	485	53
(Al,Ga)N NWs	Yes/No	/	977	54
Pt/GaN NWs	Yes/No	/	181	55
Pt/(Al,Ga) N NWs	Yes/No	/	144	56
SnO ₂ Nanosheets	Yes/No	/	3395	57
α -Ga ₂ O ₃ Nanorods	Yes/No	/	34	58
In ₂ O ₃ Nanosheets	Yes/No	/	1567	59

weight (Δw) value is regained with just 15 light pulses, and the overall synaptic weight level is relatively higher. Hence, in the subsequent learning phase, a comparable cognitive level is attainable with fewer light pulses, which opens new pathways for the advancement of artificial neural networks and brain-inspired computing technologies.

Underlying mechanism and low energy consumption

In order to better understand the working mechanism of synaptic devices, the electric field analysis between nanowires and graphene is shown in Fig. 4a–c. Specifically, Fig. 4a demonstrates the successful fabrication of the single (Al,Ga)N nanowire/graphene heterostructure. Analyses of the surface potential of the heterostructures, as measured by Kelvin probe force microscopy (KPFM) in Fig. 4b, c, reveal that the average surface potential of the (Al,Ga)N nanowire is approximately 11 mV higher than that of graphene. Hence, there is a potential difference around the nanowires covered by graphene, indicating that there is a built-in electric field at the heterostructure surface with a direction pointing from nanowire to graphene^{1,43}.

To elucidate the synaptic working mechanism of device B, the energy band structure are presented in Fig. 4d–f. When device B is irritated by the first light pulse, the photogenerated carriers are separated owing to the built-in electric field and subsequently collected under a bias (Fig. 4d). A portion of the photogenerated holes are captured by the oxygen vacancies (V_O), thereby forming quite stable V_O^{2+} complexes by the equation³³:



These complexes hinder the recombination of electron-hole (e-h) pairs, causing a significant number of the photogenerated electrons remaining within the conduction band after light off (Fig. 4e)³³. Subsequently, when the system is exposed to the second light pulse (Fig. 4f), an

increased number of photogenerated electrons and holes are accumulated by the electrodes. This accumulation leads to a higher current output than that of the previous one. This progressive increase in current with successive light stimulation mimics the behavior of synaptic plasticity, which is a fundamental attribute of synaptic devices.

The neural processing system that mimics human vision has significant advantages in low energy consumption⁴⁴. Consequently, the energy consumption (E) is a crucial parameter for assessing the performance of synaptic devices, which can be quantitatively evaluated utilizing the subsequent equation⁴⁵:

$$E = \int_{t_0}^{t_1} V \cdot I(x) dt \quad (4)$$

t_0 and t_1 represent the durations of the light being turned on and off, respectively. V is the working voltage and I is the response current of the device⁴⁶. As illustrated in Fig. S6a, E is quantified as 3.19×10^{-11} J by Eq. (4), where the pulse width and voltage are 0.5 s and 5 V, respectively. Relative to synaptic devices constructed from GaN materials or nanowire architectures^{14,29,47–50}, the featured synaptic devices demonstrate significantly reduced energy consumption (Table 1). Furthermore, the EPSC of device B exhibits a consistent increase following light stimulation (Fig. S6b). After being subjected to approximately 10^3 light pulses, the device holds a stable photocurrent with negligible fluctuations. This stability, which is sustained even after prolonged stimulation, revealing the robustness and reliability of the device during operation. Furthermore, such steadiness in response to extended light exposure highlights the synaptic resilience and potential for continuous stimulatory conditions and long-term applications.

Multifunctional nano-device for neuromorphic computing and imaging

Figure 5a shows the process of visual perception and image processing from initial input to brain interpretation, illustrating the journey of visual information from a pixelated image through the eye to the brain. A green beam represents light entering the eye, which is then transmitted via the optic nerve to the brain. As a conceptual demonstration aimed at mimicking the sensory and pre-processing functions of the human retina, a synaptic device based on (Al,Ga)N nanowire/graphene heterojunction can be configured into an 8×8 array, effectively employed for image noise suppression and contrast enhancement (Fig. 5b). After being processed by the array, the image will be utilized for further computations within a specifically designed artificial neural network (ANN). This ANN is trained using a dataset comprising 10,000 images of Arabic numerals ranging from 0 to 9, consisting of 64 input neurons, 20 hidden neurons and 10 output neurons⁵¹. Each image in this dataset undergoes the superposition of stochastic background noise generated from light signals of varying intensities. To ensure the uniformity across the dataset, these intensities are normalized to fall within a range of 0 to 0.5, thereby maintaining consistent noise levels throughout the training process of the artificial neuromorphic vision system. The correlation between the output current and the input light intensity of device A and device B is depicted through a fitted curve (Fig. S7). The entire system, encompassing both the preprocessing and recognition processes, relies on the integration of synaptic device array with the ANN architecture.

Compare with that of device A (Fig. 5c), the pre-processing of device B array significantly enhances the main characteristics of the output images by substantially reducing the background noise. Relative to the original input image, the enhanced image contrast underscores the efficacy of device B array in preliminary image processing tasks. This improvement facilitates a more discernible visualization, emphasizing the array's role in optimizing visual outputs prior to further processing steps. Furthermore, the artificial neuromorphic vision system demonstrates outstanding capabilities in noise reduction and main characteristics enhancement across kinds of noise levels (Fig. 5d and Fig. S8). The data reveal that the rate of improvement in image

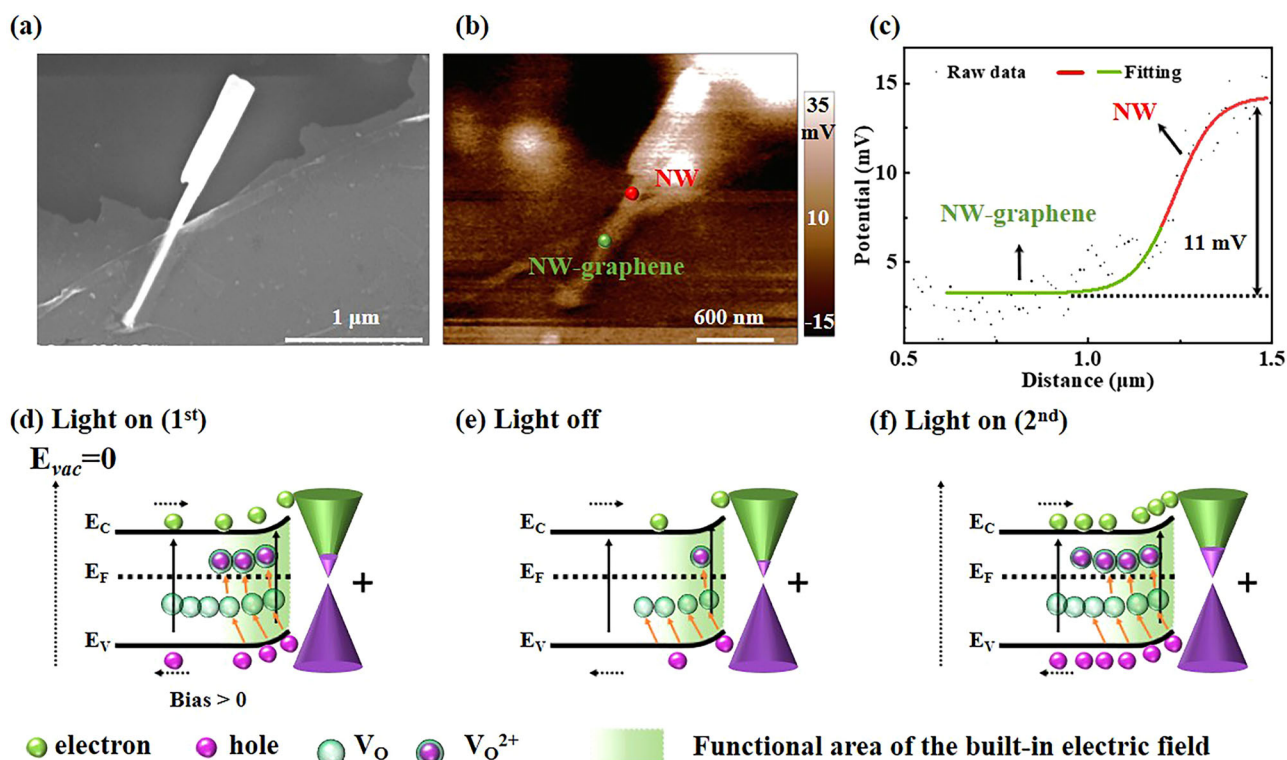


Fig. 4 | Built in electric field between nanowires and graphene. **a** SEM image of a single nanowire/graphene heterojunction. **b** Surface potential image of a single nanowire/graphene heterojunction. **c** Potential line distribution at the edge of heterostructure shows the Fermi level difference between the single nanowire and

graphene. Schematic illustration of the energy band diagrams for describing a single nanowire **(d)** under the initial light stimulation, **(e)** without light stimulation, and **(f)** under the second light stimulation.

recognition escalates with increasing background noise levels, signifying that the noise of device reduction efficacy improves under the higher noise conditions. These findings indicate that by preprocessing images with our device, it is possible to achieve the enhanced feature extraction, improved recognition accuracy and increased recognition speed with low energy consumption.

It is evident that the recognition accuracy (more than 90% after 100 training cycles) for pre-processed images by device B is significantly higher than those for pre-processed images by device A and noise images (Fig. 5e). This observation suggests that the pre-processing step enhances the ability of network to extract and interpret relevant features from the input data, thereby improving the overall classification performance. Figure 5f presents the confusion matrix that quantifies the accuracy of image recognition both prior to and subsequent to the application of noise reduction techniques. The data indicate that upon implementing noise reduction, there is a confluence between the predicted outcomes (as represented by the elements of each row) and the actual target outcomes (as denoted by the elements of each column). This alignment suggests that the classification system accurately identifies each numeral from 0 through 9, demonstrating enhanced recognition performance post-noise reduction.

Conclusion

In conclusion, a multifunctional monolithic nano-device constructed from a single (Al,Ga)N nanowire/graphene heterojunction is demonstrated for photodetection and simulation of biological synapses successfully. Thanks to the introduction of nanowire/graphene heterojunctions, the built-in electric field range is expanded, causing an effective increase in photocurrent compared to that of only a single (Al,Ga)N nanowire. This nano-device has the low-energy-consumption characteristic and the significant advantages in neural morphological network computing and recognition. Furthermore,

by exploiting the synaptic plasticity (SNDP, SFDP and SIDP) of the device, neuro-visual sensing processes for image recognition and retention can be emulated. Compared to the device with only single (Al,Ga)N nanowire and non-preprocessed data, the device with nanowire/graphene heterojunction demonstrates a significant enhancement in image recognition accuracy (>90%) and computational efficiency through the implementation of preprocessing techniques. This improvement highlights the efficacy of neuromorphic preprocessing in optimizing the visual information for subsequent analyses. The integration of sensing, memory and preprocessing multifunctionalities within a single device represents a new approach towards more efficient neuromorphic computing architectures, potentially enabling more compact and energy-efficient artificial visual processing systems.

Methods

The (Al,Ga)N nanowires are grown on the Si I substrate (Fig. 1a). They were transferred onto the top surface of 280 nm SiO₂ layer under a stereoscopic microscope (Fig. 1b), which was on an external Si II substrate. Before the transfer of nanowires, several cross marks were prepared on the SiO₂ layer via photolithography. Then scanning electron microscopy (SEM) was employed to ascertain the precise site of a single nanowire utilizing cross marks for reference. Subsequently, electrode patterns were formed at both ends of a single nanowire using electron beam lithography (EBL). Ti/Au metal electrodes were subsequently fabricated at both ends of the nanowire using electron beam evaporation and exfoliation processes, completing the preparation of device A (Fig. 1c, Table 2). Unlike device A, the process of preparing device B requires an additional step of transferring graphene before depositing metal (Fig. 1d). More details about the epitaxial growth and measurements are shown in Section 1 (Supplementary Notes) in *Supplementary Information*.

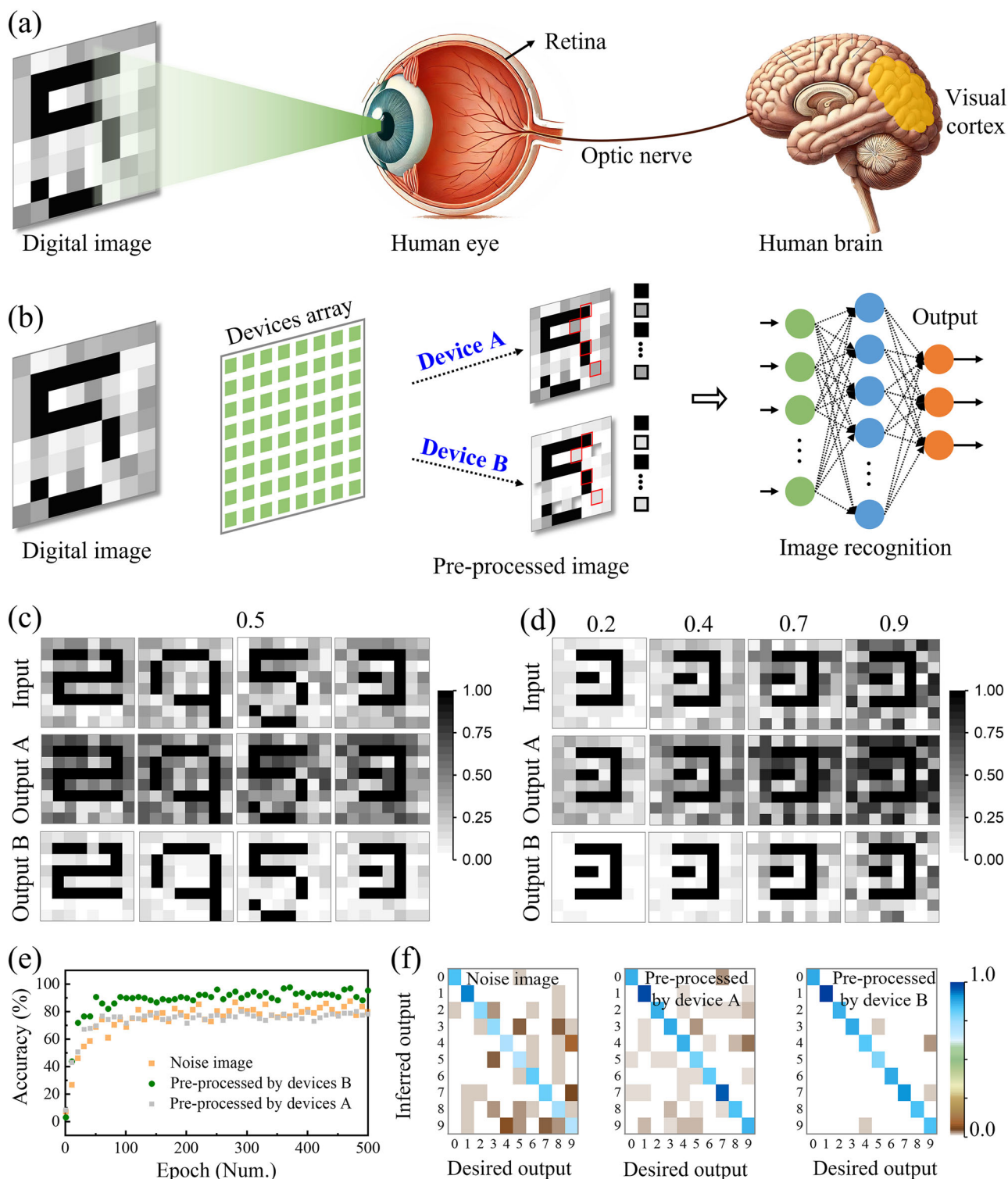


Fig. 5 | Artificial neuromorphic vision system and simulated image recognition employing the artificial synaptic devices. **a** Schematically illustrate the initial visual perception and image processing pathway from the input of an image to its cerebral interpretation. **b** A schematic diagram of an image pre-processed system that incorporates an artificial synaptic device for initial image processing, followed by an ANN for image recognition. **c** Demonstrate the noise reduction achieved using device A and device B. **d** Numerical images with and without image pre-processing

across different levels of background noise (0.2, 0.4, 0.7 and 0.9). Output A and output B correspond to device A and device B, respectively. **e** Quantify the recognition accuracy of training images, comparing conditions with and without the use of the as-prepared artificial synapse under a background noise level of 0.5. **f** Confusion matrix based on the training results with and without image pre-processing.

Table 2 | List of the devices utilized in this study

Sample	Material
Device A	Single (Al,Ga)N nanowire
Device B	Single (Al,Ga)N nanowire + graphene

Data availability

The data that support the findings of this study are available from the corresponding author upon reasonable request.

Code availability

The codes that support the findings of this study are available from the corresponding author upon reasonable request.

Received: 30 October 2024; Accepted: 11 April 2025;

Published online: 26 April 2025

References

- Zhang, Y. et al. Optoelectronic neuromorphic logic memory device based on Ga₂O₃/MoS₂ Van der Waals heterostructure with high rectification and on/off ratios. *Adv. Funct. Mater.* **34**, 2408978 (2024).
- Jiang, M. et al. Realizing bidirectional photocurrent in monolithic dual-mode device for neuromorphic vision and logically-encrypted transmission. *Adv. Funct. Mater.* 2416288 (2024).
- Zhan, T. et al. Electrical characteristics and photodetection mechanism of TiO₂/AlGaIn/GaN heterostructure-based ultraviolet detectors with a Schottky junction. *J. Mater. Chem. C* **11**, 1704–1713 (2023).
- Jiang, M., Zhao, Y., Zhou, M., Zhang, J. & Lu, S. Engineer carrier transport at (Al,Ga)N nanowire/hydrogel interface to realize self-driven ultraviolet photodetectors with switchable response speed for imaging system. *J. Alloys Compounds* **966**, 171498 (2023).
- Zhu, X. et al. Ga₂O₃-MXene nanowire networks with enhanced responsivity for Deep-UV photodetection. *ACS Appl. Nano Mater.* **6**, 2048–2062 (2023).
- Zhang, J. et al. Self-powered (In,Ga)N-nanowire-based photodetector with fast response speed for under-seawater detection. *Opt. Express* **31**, 8128–8138 (2023).
- Wang, L. et al. High-density implantable neural electrodes and chips for massive neural recordings. *Brain-X* **2**, e65 (2024).
- Kwon, J. Y. et al. Artificial sensory system based on memristive devices. *Exploration* **4**, 20220162 (2024).
- Xi, Z. Y. et al. Retina-like neuromorphic visual sensor for sensing broad-spectrum ultraviolet light. *Adv. Opt. Mater.* **12**, 2402193 (2024).
- Chen, Y. et al. All Two-dimensional Integration-Type Optoelectronic Synapse Mimicking Visual Attention Mechanism for Multi-Target Recognition. *Adv. Funct. Mater.* **33**, 2209781 (2022).
- Hong, X. et al. Two-dimensional perovskite-gated AlGaIn/GaN high-electron-mobility-transistor for neuromorphic vision sensor. *Adv. Sci.* **9**, 2202019 (2022).
- Deng, Y. et al. Large-area growth of synaptic heterostructure arrays for integrated neuromorphic visual perception chips. *Chip* **3**, 100088 (2024).
- Guo, F. H. et al. A dual-functional integration of photodetectors and artificial optoelectronic synapses on a VO₂/WO₃ heterojunction device. *Small Methods* **9**, 2400779 (2024).
- Mo, Y., Luo, B., Dong, H. & Hou, B. Light-stimulated artificial synapses based on Si-doped GaN thin films. *J. Mater. Chem. C* **10**, 13099–13106 (2022).
- Jiang, M. et al. Flexible bidirectional self-powered photodetector with significantly reduced volume and accelerated response speed based on hydrogel and lift-off GaN-based nanowires. *Fundamental Res.* **4**, 369–378 (2024).
- Sangwan, V. K. & Hersam, M. C. Neuromorphic nanoelectronic materials. *Nat. Nanotechnol.* **15**, 517–528 (2020).
- Wang, D. et al. Highly uniform, self-assembled AlGaIn nanowires for self-powered solar-blind photodetector with fast-response speed and high responsivity. *Adv. Opt. Mater.* **9**, 2000893 (2020).
- Wang, D. et al. Observation of polarity-switchable photoconductivity in III-nitride/MoS_x core-shell nanowires. *Light Sci. Appl.* **11**, 227 (2022).
- Zhang, S. et al. High responsivity GaN nanowire UVA photodetector synthesized by hydride vapor phase epitaxy. *J. Appl. Phys.* **128**, 155705 (2020).
- Zhang, L. Y. et al. Solar-blind ultraviolet photodetector based on vertically aligned single-crystalline β-Ga₂O₃ nanowire arrays. *Nanophotonics* **9**, 4497–4503 (2020).
- Zhao, Y. K. et al. Detaching (In,Ga)N nanowire films for devices requiring high flexibility and transmittance. *ACS Appl. Nano Mater.* **3**, 9943–9950 (2020).
- Tian, B. & Lieber, C. M. Nanowired bioelectric interfaces. *Chem. Rev.* **119**, 9136–9152 (2019).
- Xin, S. et al. Ultraviolet-driven metal oxide semiconductor synapses with improved long-term potentiation. *J. Mater. Chem. C* **11**, 722–729 (2023).
- Huang, C. H., Wu, C. Y., Lin, Y. F., Chou, Y. C. & Lee, K. T. Wet-etching-boosted charge storage in 1D Nitride-based systems for imitating biological synaptic behaviors. *Adv. Funct. Mater.* **33**, 2306030 (2023).
- Hua, Q. et al. Piezotronic synapse based on a single GaN microwire for artificial sensory systems. *Nano Lett.* **20**, 3761–3768 (2020).
- Xu, K. et al. An in-situ hybrid laser-induced integrated sensor system with antioxidative copper. *Int. J. Extrem. Manuf.* **6**, 065501 (2024).
- Feng, S. et al. Dual-mode conversion of photodetector and neuromorphic vision sensor via bias voltage regulation on a single device. *Adv. Mater.* **35**, 2308090 (2023).
- Han, C. et al. Light-stimulated synaptic transistor with high PPF feature for artificial visual perception system application. *Adv. Funct. Mater.* **32**, 2113053 (2022).
- Zhou, M. et al. Light-stimulated low-power artificial synapse based on a single GaN nanowire for neuromorphic computing. *Photon. Res.* **11**, 1667–1677 (2023).
- Zhou, M. et al. Realize low-power artificial photonic synapse based on (Al,Ga)N nanowire/graphene heterojunction for neuromorphic computing. *APL Photon.* **8**, 076107 (2023).
- Yang, J. Q. et al. Neuromorphic engineering: from biological to spike-based hardware nervous systems. *Adv. Mater.* **32**, e2003610 (2020).
- Guo, Z. et al. High-performance artificial synapse based on CVD-grown WSe₂ flakes with intrinsic defects. *ACS Appl. Mater. Interfaces* **15**, 19152–19162 (2023).
- Nobre, J., Safade, A., Urbano, A. & Laureto, E. A synaptic device based on the optoelectronic properties of ZnO thin film transistors. *Appl. Phys. A Mater. Sci. Process.* **129**, 203 (2023).
- Zhuang, X. et al. An amorphous native oxide shell for high bias-stress stability nanowire synaptic transistor. *Adv. Sci.* **10**, 2302516 (2023).
- Wang, C. Y. et al. Strain-insensitive viscoelastic perovskite film for intrinsically stretchable neuromorphic vision-adaptive transistors. *Nat. Commun.* **15**, 3123 (2024).
- Wang, J. et al. Piezo-phototronic effect modulated optoelectronic artificial synapse based on a-Ga₂O₃/ZnO heterojunction. *Nano Energy* **120**, 109128 (2024).
- Liu, T. et al. Multifunctional organic vertical photodiodes for photo-detection and photo-synapse enabled by modulation of the interface energy barrier. *Adv. Opt. Mater.* **10**, 2201104 (2022).
- Zhang, F., Li, C., Li, Z., Dong, L. & Zhao, J. Recent progress in three-terminal artificial synapses based on 2D materials: from mechanisms to applications. *Microsyst. Nanoeng.* **9**, 16 (2023).
- Shrivastava, S., Keong, L. B., Pratik, S., Lin, A. S. S. & Tseng, T.-Y. Fully photon controlled synaptic memristor for neuro-inspired computing. *Adv. Electron. Mater.* **9**, 2201093 (2023).

40. Yang, W. H., Kan, H., Shen, G. Z. & Li, Y. A network intrusion detection system with broadband $\text{WO}_{3-x}/\text{WO}_{3-x}\text{-Ag}/\text{WO}_{3-x}$ optoelectronic memristor. *Adv. Funct. Mater.* **34**, 2312885 (2024).
41. Sunny, A. & Thamankar, R. Emulating Ebbinghaus forgetting behavior in a neuromorphic device based on low dimensional h-BN. *AIP Adv.* **14**, 085010 (2024).
42. Hu, Y. X. et al. Flexible optical synapses based on $\text{In}_2\text{Se}_3/\text{MoS}_2$ heterojunctions for artificial vision systems in the near-infrared range. *ACS Appl. Mater. Interfaces* **14**, 55839–55849 (2022).
43. Wang, X. et al. Enhancing the performance of self-powered deep-ultraviolet photoelectrochemical photodetectors by constructing $\alpha\text{-Ga}_2\text{O}_3@ \alpha\text{-Al}_2\text{O}_3$ core-shell nanorod arrays for solar-blind imaging. *Appl. Surf. Sci.* **648**, 159022 (2024).
44. Sun, T. et al. Artificial intelligence meets flexible sensors: emerging smart flexible sensing systems driven by machine learning and artificial synapses. *Nano-Micro Lett.* **16**, 14 (2023).
45. Li, X., Li, S., Tang, B., Liao, J. & Chen, Q. A Vis-SWIR photonic synapse with low power consumption based on $\text{WSe}_2/\text{In}_2\text{Se}_3$ ferroelectric heterostructure. *Adv. Electron. Mater.* **8**, 2200343 (2022).
46. Wu, W. Q., Wang, C. F., Han, S. T. & Pan, C. F. Recent advances in imaging devices: image sensors and neuromorphic vision sensors. *Rare Met.* **43**, 5487–5515 (2024).
47. Zha, C. F., Luo, W., Zhang, X., Yan, X. & Ren, X. M. Low-consumption synaptic devices based on Gate-All-Around in as nanowire field-effect transistors. *Nanoscale Res. Lett.* **17**, 101 (2022).
48. Shen, C. et al. ZnO nanowire optoelectronic synapse for neuromorphic computing. *Nanotechnology* **33**, 065205 (2022).
49. Li, X. et al. Complementary photo-synapses based on light-stimulated porphyrin-coated silicon nanowires field-effect transistors (LPSNFET). *Small* **17**, 2101434 (2021).
50. Qi, H. & Wu, Y. Synaptic plasticity of TiO_2 nanowire transistor. *Microelectron. Int.* **37**, 125–130 (2020).
51. Lu, Feng & Lu, W. Handwritten numeral recognition based on DCT coefficients and neural network. *Int. Conf. Neural Netw. Brain* **1**, 219–221 (2005).
52. Feng, S. et al. Dual-mode conversion of photodetector and neuromorphic vision sensor via bias voltage regulation on a single device. *Adv. Mater.* **35**, 2308090 (2023).
53. Jiang, M. et al. Self-powered photoelectrochemical (Al,Ga)N photodetector with an ultrahigh ultraviolet/visible reject ratio and a quasi-invisible functionality for 360° omnidirectional detection. *ACS Photon.* **8**, 3282–3290 (2021).
54. Jiang, M. et al. Flexible self-powered photoelectrochemical photodetector with ultrahigh detectivity, ultraviolet/visible reject ratio, stability, and a quasi-invisible functionality based on Lift-Off Vertical (Al,Ga)N nanowires. *Adv. Mater. Interfaces* **9**, 2200028 (2022).
55. Fang, S. et al. Tuning the charge transfer dynamics of the nanostructured GaN photoelectrodes for efficient photoelectrochemical detection in the ultraviolet band. *Adv. Funct. Mater.* **31**, 2103007 (2021).
56. Wang, D. et al. Pt/AlGaIn nanoarchitecture: toward high responsivity, self-powered ultraviolet-sensitive photodetection. *Nano Lett.* **21**, 120–129 (2020).
57. Yu, H. et al. One stone, three birds: SnO_2 nanosheet arrays toward self-powered visible-blind UV photodetection with high responsivity and rejection ratio. *Adv. Opt. Mater.* **12**, 2301460 (2024).
58. Junhua, Z. et al. Solar-blind ultraviolet photodetection of an $\alpha\text{-Ga}_2\text{O}_3$ nanorod array based on photoelectrochemical self-powered detectors with a simple, newly-designed structure. *J. Mater. Chem. C* **7**, 6867–6871 (2019).
59. Zhang, M. et al. Ultrathin In_2O_3 nanosheets toward high responsivity and rejection ratio visible-blind UV photodetection. *Small* **19**, 2205623 (2023).

Acknowledgements

This research was financially supported by National Natural Science Foundation of China (No. 62174172), China Postdoctoral Science Foundation (Nos. 2023TQ0238 and 2023M742560), Key Research Program of Frontier Sciences, CAS (No. ZDBS-LY-JSC034), Suzhou Fundamental Research Project (SSD2024003), Key Laboratory of Nanodevices of Jiangsu Province (No. ZS2302), Jiangsu Key Disciplines of the Fourteenth Five-Year Plan (No. 2021135), Jiangsu Funding Program for Excellent Postdoctoral Talent (2024ZB566), Science and Technology Youth Talent Project of Jiangsu Province (JSTJ-2024-016), and the Students' Innovation and Entrepreneurship Foundation of USTC (CY2024X003B). The authors are grateful for the technical support for Nano-X, Platform for Nanofabrication Facility (SNFF) and for Characterization & Test of SINANO, Chinese Academy of Sciences (CAS).

Author contributions

M.Z. and M.J. performed all device fabrication experiments, conducted device measurements, and undertook the associated data collection and analyses. Y.K.Z. conceived the research idea and guided the work. L.B.Y., M.Z. and J.Y.Z. performed the SEM measurements. M.Z., Y.K.Z., and J.Y.Z. performed the mechanism studies. M.Z., M.J. and Y.K.Z. prepared the original draft of the manuscript. J.Y.Z., Y.K.Z., S.L.L., and L.F.B. were responsible for securing funding and project administration. Y.K.Z. executed all MBE experiments. M.Z., C.Y.S., and K.X. contributed to the methodology and visualization of this study. M.Z., C.Y.S., and J.Y.Z. carried out the investigation. All authors have reviewed and approved the manuscript.

Competing interests

The authors declare no competing interests.

Additional information

Supplementary information The online version contains supplementary material available at <https://doi.org/10.1038/s43246-025-00803-5>.

Correspondence and requests for materials should be addressed to Chaoyun Song, Jianya Zhang, Shulong Lu or Yukun Zhao.

Peer review information *Communications Materials* thanks Jung Ho Yoon and the other, anonymous, reviewer(s) for their contribution to the peer review of this work. Primary Handling Editors: Sunkook Kim and Aldo Isidori.

Reprints and permissions information is available at <http://www.nature.com/reprints>

Publisher's note Springer Nature remains neutral with regard to jurisdictional claims in published maps and institutional affiliations.

Open Access This article is licensed under a Creative Commons Attribution-NonCommercial-NoDerivatives 4.0 International License, which permits any non-commercial use, sharing, distribution and reproduction in any medium or format, as long as you give appropriate credit to the original author(s) and the source, provide a link to the Creative Commons licence, and indicate if you modified the licensed material. You do not have permission under this licence to share adapted material derived from this article or parts of it. The images or other third party material in this article are included in the article's Creative Commons licence, unless indicated otherwise in a credit line to the material. If material is not included in the article's Creative Commons licence and your intended use is not permitted by statutory regulation or exceeds the permitted use, you will need to obtain permission directly from the copyright holder. To view a copy of this licence, visit <http://creativecommons.org/licenses/by-nc-nd/4.0/>.

© The Author(s) 2025